Ann. Geophys., 26, 3235–3252, 2008
www.ann-geophys.net/26/3235/2008/


Annales Geophysicae

# Gravity wave and tidal influences on equatorial spread F based on observations during the Spread F Experiment (SpreadFEx)

**D. C. Fritts[1], S. L. Vadas[1], D. M. Riggin[1], M. A. Abdu[2], I. S. Batista[2], H. Takahashi[2], A. Medeiros[3], F. Kamalabadi[4], H.-L. Liu[5], B. G. Fejer[6], and M. J. Taylor[6]**

[1]NorthWest Research Associates, CoRA Division, Boulder, CO, USA
[2]Instituto Nacional de Pesquisas Espaciais (INPE), San Jose dos Campos, Brazil
[3]Universidade Federal de Campina Grande. Campina Grande. Paraiba. Brazil
[4]University of Illinois, Champaign, IL, USA
[5]National Center for Atmospheric research, Boulder, CO, USA
[6]Utah State University, Logan, UT, USA

Received: 15 April 2008 – Revised: 7 August 2008 – Accepted: 7 August 2008 – Published: 21 October 2008

**Abstract.** The Spread F Experiment, or SpreadFEx, was performed from September to November 2005 to define the potential role of neutral atmosphere dynamics, primarily gravity waves propagating upward from the lower atmosphere, in seeding equatorial spread F (ESF) and plasma bubbles extending to higher altitudes. A description of the SpreadFEx campaign motivations, goals, instrumentation, and structure, and an overview of the results presented in this special issue, are provided by Fritts et al. (2008a). The various analyses of neutral atmosphere and ionosphere dynamics and structure described in this special issue provide enticing evidence of gravity waves arising from deep convection in plasma bubble seeding at the bottomside F layer. Our purpose here is to employ these results to estimate gravity wave characteristics at the bottomside F layer, and to assess their possible contributions to optimal seeding conditions for ESF and plasma instability growth rates. We also assess expected tidal influences on the environment in which plasma bubble seeding occurs, given their apparent large wind and temperature amplitudes at these altitudes. We conclude 1) that gravity waves can achieve large amplitudes at the bottomside F layer, 2) that tidal winds likely control the orientations of the gravity waves that attain the highest altitudes and have the greatest effects, 3) that the favored gravity wave orientations enhance most or all of the parameters influencing plasma instability growth rates, and 4) that gravity wave and tidal structures acting together have an even greater potential impact on plasma instability growth rates and plasma bubble seeding.

*Correspondence to:* D. C. Fritts
(dave@cora.nwra.com)

**Keywords.** Ionosphere (Equatorial ionosphere; Ionosphere-atmosphere interactions; Plasma convection) – Meteorology and atmospheric dynamics (Middle atmosphere dynamics; Thermospheric dynamics; Waves and tides)

## 1 Introduction

The primary goal of the Spread F Experiment (SpreadFEx) was to test the theory that gravity waves (GWs) play a key role in the seeding of equatorial spread F (ESF), Rayleigh-Taylor instability (RTI), and plasma bubbles extending to much higher altitudes. To achieve this goal, SpreadFEx comprised correlative ground-based and satellite measurements of the neutral atmosphere and ionosphere spanning two "moon-down" periods extending from late September to early November 2005. SpreadFEx ground-based measurements were performed with a suite of airglow cameras, VHF and meteor radars, digisondes, and GPS receivers at a number of fixed and temporary sites in Brazil. Additional correlative data were collected by GOES 12, with the GUVI instrument aboard the TIMED satellite, and at the Jicamarca Radio Observatory in Peru. Together, these measurements provided 1) sensitivity to the major sources of GWs in the tropical lower atmosphere, 2) characterization of the environment through which GWs propagated to higher altitudes, 3) quantification of GW spatial scales, frequencies, amplitudes, and orientations at intermediate (neutral atmospheric) and higher (ionospheric) altitudes, and 4) a spatial and temporal characterization of coincident plasma perturbations and plasma bubbles penetrating to higher altitudes. Additional

key components of our SpreadFEx analyses include the use of campaign data 5) to assess the potential for GWs reaching the bottomside F layer to contribute sufficient perturbations of neutral and plasma parameters to impact plasma instability growth rates and 6) to assess the growth rate enhancements implied by these perturbations and evaluate their impact on plasma bubble seeding. Together, the various SpreadFEx measurements yielded one of the most comprehensive data set for studies of equatorial neutral-plasma coupling and instability seeding assembled to date. An overview of SpreadFEx and a summary of our various data analyses reported in this special issue are provided by Fritts et al. (2008a, hereafter F08a).

Collectively, our various data analyses address all of the links between deep tropical convection and plasma bubble seeding at the bottomside F layer. GOES 12 data are employed by Vadas et al. (2008a) and São Sabbas et al. (2008) to characterize the spatial and temporal scales of deep convection that excite GWs penetrating to high altitudes and the convective links to sprites, respectively. GW scales observed in airglow layers in the mesosphere and lower thermosphere (MLT) by Taylor et al. (2008, hereafter T08) and Wrasse et al. (2008) are linked to convection at lower altitudes and shown to penetrate to much higher altitudes under suitable propagation conditions by Vadas et al. (2008a, b, hereafter V08a and V08b), Vadas and Fritts (2008, hereafter VF08), and Fritts and Vadas (2008, hereafter FV08). Takahashi et al. (2008) also note a close correlation between GW spatial scales in the MLT and plasma bubble scales seen in 6300 Å emissions at the F layer peak. Additional evidence of GW spatial and temporal scales and amplitudes in the MLT and extending to the bottomside F layer and above is provided by the airglow GW momentum flux analysis by Vargas et al. (2008), tomographic inversions of TIMED/GUVI data yielding cross sections of field aligned electron densities above ∼100 km by Kamalabadi et al. (2008), and evidence of GW oscillations, electron density fluctuations, and vertical phase progression in digisonde and GPS electron density and total electron content (TEC) measurements shown by F08a, Takahashi et al. (2008), and Abdu et al. (2008). These various neutral atmosphere and plasma measurements are employed in this paper to evaluate plausible GW scales, perturbations, and orientations and their potential impacts on neutral and plasma parameters at the bottomside F layer. Our results are also employed by Abdu et al. (2008) to evaluate specific impacts on various estimates of plasma instability growth rates and by Kherani et al. (2008) as initial conditions for 3-D plasma simulations of potential GW seeding of plasma bubbles. Interferometric analysis of SpreadFEx VHF radar data by Rodrigues et al. (2008) provides evidence of plasma instabilities also arising on spatial scales that are too small to be attributed to GWs propagating from below.

To play a role in seeding plasma instabilities at the bottomside F layer, GWs arising from convection must be excited with sufficiently large spatial scales and high frequencies to be able to penetrate the strong and variable winds occurring throughout the lower and middle atmosphere (Vadas and Fritts, 2004, 2006; Vadas, 2007, hereafter VF04, VF06, and V07). These include the quasi-biennial oscillation in the zonal wind in the lower stratosphere, the semiannual oscillation with anti-correlated zonal wind maxima near the stratopause and mesopause (∼50 and 90 km), and apparently large and variable tidal and planetary wave (PW) winds that become increasingly important in the mesosphere and lower thermosphere (MLT). Tidal winds and temperature fluctuations, in particular, may be $\sim 100\,\mathrm{ms}^{-1}$ and ∼100 K or larger in the lower thermosphere and are expected to themselves play a role in defining conditions under which plasma instabilities can arise (Fritts et al., 2008b, hereafter F08b; Abdu et al., 2008; Kherani et al., 2008). The GWs that reach the bottomside F layer must also be excited at sufficiently large amplitudes, grow in amplitude due to density decreases, avoid refraction to small spatial scales or low intrinsic frequencies, and escape significant viscous dissipation to allow them to arrive at the bottomside F layer with sufficient amplitudes to influence plasma instability growth rates. All these requirements imply the excitation of GWs arising from the deepest convection that have large horizontal and vertical scales, high intrinsic frequencies, and attain significant amplitudes prior to viscous dissipation (Vadas and Fritts, 2005, hereafter VF05; V07; FV08).

The plasma instability growth rates evaluated by Abdu et al. (2008) and Kherani et al. (2008) depend in various ways on neutral winds, horizontal and vertical plasma drifts, plasma density gradients, electric and magnetic fields, conductivities, collision frequencies, and perturbations scales and orientations. GWs at bottomside F-layer altitudes will act to modulate these parameters, and the associated growth rates, to varying degrees and with various correlations, depending on GW amplitudes, scales, intrinsic frequencies, orientations, and potential superpositions. Our goal here is to consider various scenarios for GW perturbations to the parameters influencing plasma instability growth rates based on our best estimates of the GW parameters that are suggested at bottomside F-layer altitudes by the SpreadFEx data analyses and theoretical efforts reported in this special issue. We summarize in Sect. 2 the GW characteristics in the lower and middle atmosphere and at bottomside F-layer altitudes implied by our SpreadFEx data analyses and related theoretical studies. Section 3 considers the impacts of superposed large-scale tidal wind and temperature fields and smaller-scale GW structures, orientations, amplitudes, and gradients on parameters influencing plasma instability growth rates. Our summary and conclusions are provided in Sect. 4.

## 2 GW characteristics inferred from SpreadFEx and related studies

### 2.1 GW amplitudes, scales, and orientations in the lower and middle atmosphere

Our SpreadFEx measurements in the neutral atmosphere have yielded a number of indications of the sources, character, and morphology of the GWs penetrating into the thermosphere during the SpreadFEx campaign. The GW studies by T08, V08b, and Wrasse et al. (2008) all provide persuasive evidence that the dominant sources of GWs at airglow altitudes during SpreadFEx generally occurred to the west of our airglow observations at Brasilia, Cariri, and Cachoeira Paulista. This is true both for the smaller horizontal wavelengths that are most prevalent in airglow data, and which appear to arise from sources nearer the observation site in cases where these motions are not ducted, and for the larger horizontal wavelengths that can be ray traced to potential sources at considerable distances. The sources of the larger GW horizontal wavelengths were suggested by V08b to be the deep convection identified in GOES 12 data by São Sabbas et al. (2008) and V08a. The strong preference for eastward GW propagation during SpreadFEx at our measurement sites is exhibited with Keograms of OH airglow intensity at Brasilia and Cariri on the night beginning 1 October in Fig. 1. Though not shown explicitly, movement of structures at both sites was generally eastward, but is slower and at ∼20 to 150-km zonal wavelengths at Brasilia and faster and at ∼50 to 300-km zonal wavelengths at Cariri.

GW propagation directions were analyzed more quantitatively by T08 and Wrasse et al. (2008) and were found to have an eastward component for every event analyzed throughout the measurement campaign. Predominant propagation directions at Brasilia were slightly north of east and towards the southeast, with slightly more directional (but still eastward) isotropy observed at Cariri, except for a significant maximum towards the northeast (see Fig. 1 of Wrasse et al., 2008). While our SpreadFEx GW airglow observations indicate a preference for eastward propagation from deep convective sources to the west of our observations, they cannot provide any information on the relative excitation and occurrence of eastward and westward propagation at airglow altitudes. Such an assessment would require symmetric measurements east and west of the same convective sources. But as we have shown previously (VF04; VF06; V07), GW propagation and potential anisotropy at higher altitudes is strongly influenced by the winds at lower altitudes. We anticipate, however, that those GWs having the largest spatial scales and highest intrinsic frequencies will have sufficiently high phase speeds to not be strongly affected by winds at lower altitudes, despite how these winds may impact the smaller-scale and lower-frequency GWs more likely to be observed at airglow altitudes significant distances from their sources. Thermospheric winds are nevertheless anticipated to strongly influence the ultimate penetration altitudes of even those GWs having the largest scales and highest frequencies. These topics are addressed for general lower atmospheric sources in this special issue by FV08, and VF08 demonstrate a new method for reconstruction of GW fields arising from convective sources in variable environments. The implications for GW contributions to instability processes are discussed in more detail below.

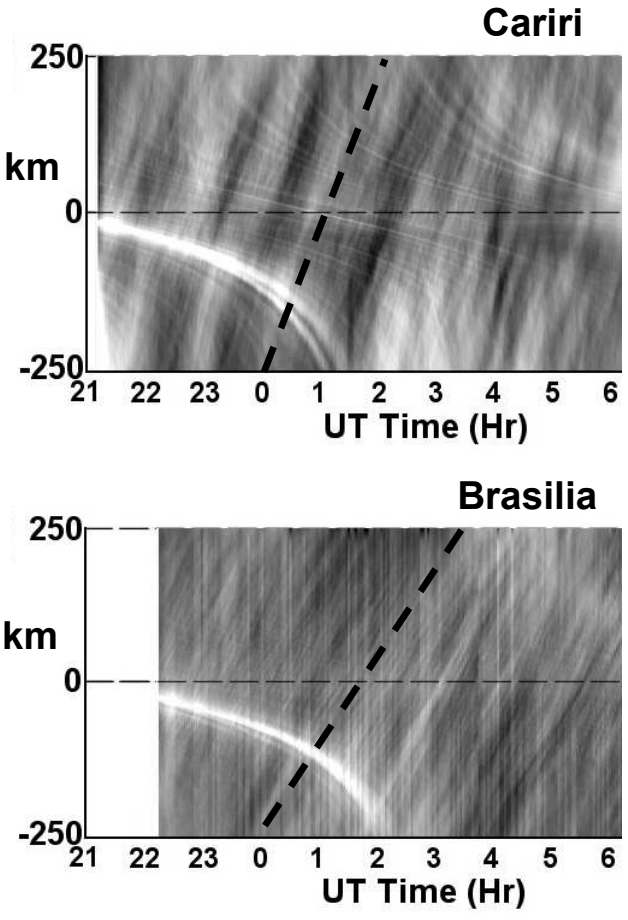


**Fig. 1.** Keograms prepared from east-west slices of OH airglow emissions obtained at Cariri (top) and Brasilia (bottom) on 1 October 2005. Note that movement of structures at both sites is generally eastward, but is faster and at ∼50 to 300-km zonal wavelengths at Cariri and slower and at ∼20 to 150-km zonal wavelengths at Brasilia. Typical eastward phase speeds for each site are shown with the heavy dashed lines in each panel.

GW amplitudes and momentum fluxes for a number of GWs observed at larger horizontal wavelengths were assessed by Vargas et al. (2008) and V08b using spectral and deterministic methods, respectively. Peak airglow intensity perturbations for GW horizontal wavelengths of ∼60 to 160 km were found to be in the range ∼2 to 7%, implying horizontal perturbation velocities in the range $u'_h$∼3 to 10 ms$^{-1}$ and momentum fluxes of $<u'_h w'>$∼1

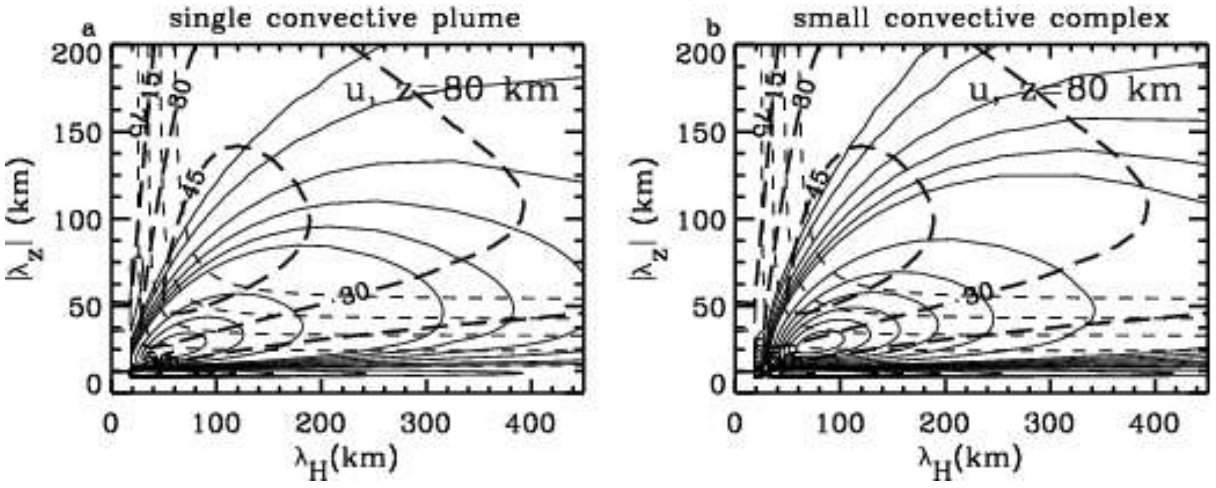


**Fig. 2.** 2-D distributions of maximum GW horizontal velocities at 80 km from the convective GW source spectra for a single plume (left) and a 3-plume convective complex each having the same scales (right) inferred as a "best fit" for the GWs reverse ray traced by V08b. In each case, maximum inferred plume updrafts are 40 $ms^{-1}$. Solid contours are at 0.5, 1, 2, 3, 4, and 5 $ms^{-1}$, and then at 5 $ms^{-1}$ intervals thereafter. Heavy dashed lines are vertical group velocities (in $ms^{-1}$), and light dashed lines are horizontal phase speeds. We also note that amplitudes at the largest scales may be uncertain by ∼2 because of the discretization of the initial GW spectrum and the averaging over discrete responses required to define these distributions.

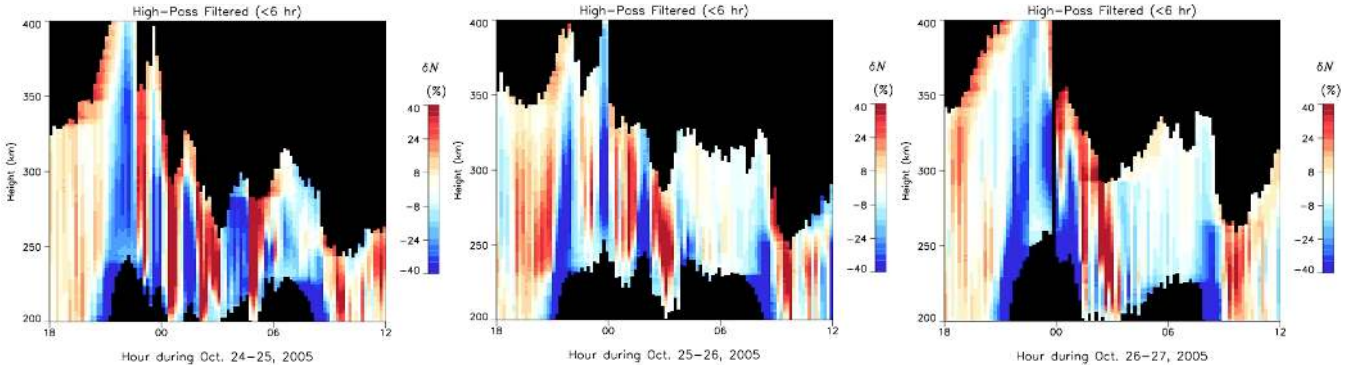


**Fig. 3.** Electron density fluctuations computed from the digisonde data for the three nights of 24 to 27 October 2005 from 18:00 to 12:00 UT. Note the large electron density fluctuations (up to ∼40%), with oscillation periods of ∼20 min to 2 h and apparent downward phase progressions at altitudes of ∼280 km and below. Note that large $K_p$ values (∼4) occurred only on 25 October, with smaller values the following days.

to 10 $m^2 s^{-2}$ (T08; V08b, assuming a Krassovsky ratio of $\eta=(I'/I)/(T'/T)\sim 3.3$). These GW wavelength, amplitude, and momentum flux estimates, together with reverse ray tracing to infer distances from likely convective sources, allowed estimates of the spatial and temporal scales of the convective plumes that likely generated these GWs (V08b). Hence, they also enabled us to constrain the 2-D GW spectrum implied by the Fourier-Laplace description of convective sources (FV04; FV06) and extrapolate to estimates of GW amplitudes arising from the same convection, but at larger vertical wavelengths expected to penetrate to much higher altitudes. This appears to be our best method for estimating the amplitudes of large-scale GWs arising from convection that are able to propagate to the bottomside F layer.

2-D distributions of maximum GW horizontal velocities with horizontal and vertical wavelengths that are consistent with the GW observations by T08, the reverse ray tracing by V08b, and the 2-D spectrum employed by VF08 are shown in Fig. 2. These display expected GW amplitudes arising from a single plume (left) and a complex of three identical plumes (right) at 80 km assuming zero mean winds. Implied maximum GW horizontal velocities are as large as ∼20 $ms^{-1}$ for horizontal and vertical wavelengths centered near ∼60 and 25 km, respectively, for a single plume. For a convective complex (Fig. 3b), maximum GW horizontal velocities at ∼80 km are ∼35 $ms^{-1}$ for horizontal and vertical wavelengths centered near ∼80 and 30 km, respectively. Maximum GW horizontal velocities are significantly smaller at

the larger wavelengths expected to reach the bottomside F layer (FV08). Nevertheless, we see that maximum velocities of ∼1 to 2 $ms^{-1}$ are expected at vertical and horizontal wavelengths of 150 km and ∼200 to 400 km, respectively, arising from a single plume, with amplitudes ∼2 times larger in response to a small convective complex. Amplitudes at vertical wavelengths of ∼200 km are ∼2 times smaller for both single plumes and small complexes. Thus, GW momentum fluxes of ∼1 to 5 $m^2s^{-2}$ are likely also representative maximum values due to such forcing. Hence we will use horizontal velocity and momentum flux values of 1 $ms^{-1}$ and 1 $m^2 s^{-2}$ as nominal (conservative) upper limits to guide our estimates of potential GW effects at higher altitudes, and for comparison with amplitude estimates based on various electron density measurements, in the remainder of this paper. We also anticipate a factor of ∼2 uncertainty in the inferred GW amplitudes, however, due to the coarse discretization of the spectrum required for this computation and the extrapolation of the GW spectrum to larger vertical wavelengths and intrinsic frequencies than were observed directly in OH airglow at Brasilia and Cariri.

### 2.2 GW amplitudes, scales, and orientations in the ionosphere

As noted above, a number of authors have interpreted electron density fluctuations in the thermosphere as evidence of neutral GWs also inducing plasma density fluctuations. The purpose of this section is to review the evidence for such fluctuations in our SpreadFEx data and to estimate the magnitudes of these plasma (and neutral) fluctuations in order to assess their potential to modulate plasma quantities that contribute to the various plasma instability processes at the bottomside F layer examined by Abdu et al. (2008) and Kherani et al. (2008) in this special issue.

Several data sets have provided evidence of GW amplitudes, spatial scales, and observed periods at the bottomside F layer during our SpreadFEx measurement campaign. These include a digisonde and a 30 MHz VHF radar at São Luis, a second digisonde at Fortaleza, a cluster of GPS instrumentation throughout eastern Brazil, and the GUVI instrument aboard the TIMED satellite. As these instruments typically provide estimates of plasma quantities, however, we will first outline the theory that allows us to quantify the relations between neutral and plasma fluctuations. We will then consider the implications of plasma measurements for GW amplitudes and influences at the bottomside F layer.

#### 2.2.1 Relations between neutral and plasma quantities

To relate the observed electron density perturbations to neutral density perturbations, we assume mean neutral and electron density profiles of the form

$$\rho(z) = \rho e^{-z/H} \tag{1}$$

and

$$\rho_e(z) = \rho_e e^{z/H_e}, \tag{2}$$

where $H$ and $H_e$ are the respective (positive) neutral and electron density scale heights. We then assume GW velocity, pressure, potential temperature, and neutral and electron (and ion) density perturbations of the form

$$(u', v', w', p'/p, \theta'/\theta, \rho'/\rho, \rho_e'/\rho_e) \sim \exp[i(kx + ly + mz - \omega t) + z/2H] \tag{3}$$

where primes denote perturbations and $\boldsymbol{k}=(k, l, m)$ is the GW wavenumber vector. Also assuming that the plasma moves with the GW perturbation wind field and that there are no chemical or electrodynamic processes that also impact plasma densities, the electron (or ion) continuity equation, $d\rho_e/dt=0$, may be written as

$$\rho_e'/\rho_e = ku'/\omega + lv'/\omega + mw'/\omega - iw'/\omega H_e \tag{4}$$

Employing the energy conservation and continuity equations (Fritts and Alexander, 2003)

$$i\omega\theta'/\theta = (N^2/g)w' \tag{5}$$

and

$$i\omega\rho'/\rho = iku' + ilv' + (im - 1/2H)w' \tag{6}$$

we obtain

$$(\rho_e'/\rho_e)/(\rho'/\rho) = 1 - (g/N^2)(1/2H + 1/H_e) \tag{7}$$

Finally, employing the relation $N^2H/g+gH/c_s^2=1$ (Fritts and Alexander, 2003), or $N^2=(g/H)(1-1/\gamma)$, with $c_s^2=\gamma gH$ and $\gamma=c_p/c_v=1.4$, we obtain

$$(\rho_e'/\rho_e)/(\rho'/\rho)=-(2-\gamma)/2(\gamma-1)-\gamma H/(\gamma-1)H_e \tag{8}$$

Additionally, from the GW polarization relations (Fritts and Alexander, 2003) we obtain relations for vertical and horizontal perturbation velocities in terms of fractional densities

$$w' \sim (g\omega/N^2)\rho'/\rho, \tag{9}$$

or in a form that is more commonly used

$$u_h'=-(m/k_h)w'\sim(m/k_h)(g\omega/N^2)\rho'/\rho=\beta(g/N)\rho'/\rho. \tag{10}$$

In the above, $u_h'$ and $w'$ are the horizontal and vertical GW perturbation velocities, $\omega=k_h(c-U_n)$ is the GW intrinsic frequency, $k_h=(k^2+l^2)^{1/2}=2\pi/\lambda_h$ and $m=2\pi/\lambda_z$ are the GW horizontal and vertical wavenumbers, $c$ and $U_n$ are the GW horizontal phase speed and the neutral mean wind in the direction of propagation, $\lambda_h$ and $\lambda_z$ are the GW horizontal and vertical wavelengths, and $\beta\sim(1-\omega^2/N^2)^{1/2}\sim1$ for hydrostatic and small-scale GWs. With our degree of approximation, Eq. (9) is accurate for all GWs in the TI, whereas $\beta\sim1$ in Eq. (10) only when $\lambda_h^2 \ll 16\,\pi^2\,H^2$ and $\omega^2 \ll N^2$. These are reasonable assumptions at lower altitudes, but they are less

accurate where GW vertical wavelengths exceed ∼100 km and intrinsic frequencies exceed $\omega \sim N/2$, as we expect to occur in response to increasing kinematic viscosity and thermal diffusivity in the TI (VF05; VF06; V07; FV08). When $\omega > N/1.4$ and GW scales increase, $\beta < 0.7$ and approximations appropriate for the lower atmosphere lead to overestimates of $u'_h$ based on density measurements.

Under minimum solar forcing conditions, thermospheric temperatures above ∼200 km are ∼600 K and gradients are small, such that $N^2 \sim 1.6 \times 10^{-4}\,\mathrm{s}^{-2}$ and the buoyancy period is $T_b \sim 8$ min. For mean solar forcing conditions and a thermospheric temperature of ∼1000 K, $N^2 \sim 10^{-4}\,\mathrm{s}^{-2}$ and the buoyancy period is $T_b \sim 10$ min. Thus we should expect typical GW intrinsic periods of $T_i = 2\pi/\omega \sim 10$ to 60 min to have been dominant during SpreadFEx (V07; FV08; VF08). We also expect neutral and electron density scale heights of $H \sim 20$ to 30 km and $H_e \sim 30$ to 100 km, such that the ratio of fractional electron to neutral density fluctuations in Eq. (8) is $(\rho'_e/\rho_e)/(\rho'/\rho) \sim 3$ to 5. During maximum solar forcing, $T \sim 1500$ K, $N^2 \sim 0.6 \times 10^{-4}\,\mathrm{s}^{-2}$, $H \sim 50$ km, and $u'_h$ and $w'$ would be comparable to, or slightly larger than, their values at solar minimum for the same density perturbations.

### 2.2.2 Implications of plasma measurements for GW parameters

A data set that is highly relevant to our attempts to relate neutral and plasma perturbations in the F layer was obtained by Dynamics Explorer 2 (DE-2) at mid-latitudes and altitudes of ∼250 to 300 km during final orbital decay. These data included combined direct measurements of neutral and plasma densities and velocities extending to very small spatial scales (Earle et al., 2008). The results indicate unambiguously the presence of large-scale and large-amplitude GWs at these altitudes that appear to agree closely with the predictions by FV08. Apparent GW horizontal wavelengths were seen to be confined to scales of ∼100 km or greater, neutral and electron densities were seen to be anti-correlated (see Eq. 8 above), with fractional electron density perturbations larger by ∼3 times, and neutral and plasma velocities were observed to be largely in quadrature with the observed neutral and electron density fluctuations. But possibly the most interesting result of the analysis of these data was the inference of very large vertical (and horizontal) velocity perturbations, $\sim 20\,\mathrm{m\,s}^{-1}$ or larger, that appears to validate the estimates of comparable GW amplitudes from our various SpreadFEx data sets. Separate Doppler radar wind measurements with the new Poker Flat Incoherent Scatter Radar (PFISR), though in a very different geophysical environment, also yielded significant horizontal perturbation velocities of $\sim 50\,\mathrm{m\,s}^{-1}$ at ∼200 km altitudes that were attributed to GWs by Vadas and Nicolls (2008). Thus, there are many data sets, both qualitative and quantitative, having perturbations spanning a range of spatial and temporal scales in the TI that can be attributed to GWs likely arising from lower atmosphere sources.

Electron density data collected with the digisonde at São Luis from 00:00 UT on 24 October to 24:00 UT on 27 October 2005 during the second measurement interval of SpreadFEx are shown in the upper panel of Fig. 8 of our SpreadFEx overview (F08a). These exhibit both the normal diurnal modulation of electron densities and features specific to equatorial latitudes, in particular the strong elevation of the F layer accompanying the pre-reversal enhancement (PRE) of the electric field and successive vertical excursions of the bottomside F layer. The excursions were as large as ∼10 to 100 km (peak-to-peak) and had periods of ∼20 min to 2 h. Electron density fluctuations computed from the digisonde data from São Luis from 18:00 to 12:00 UT for all three nights are shown in Fig. 3. The large altitude excursions and electron density fluctuations suggest large vertical velocities of ∼20 to $40\,\mathrm{m\,s}^{-1}$ inferred from these data by Abdu et al. (2008). Caution is warranted in attempting to quantify GW perturbations from these measurements, however, as we do not have simultaneous neutral wind or density measurements, and we cannot account for possible influences of chemical, electrodynamic, or plasma instability processes (including topside bubbles that may impact inferred GW neutral amplitudes). Nevertheless, we will assume inferred amplitudes are qualitatively correct for the purposes of comparing with predictions and inferences from other measurements, given their qualitative agreement with the direct measurements using DE-2 data by Earle et al. (2008).

The electron densities also suggest both a tendency for downward phase progression of these fluctuations (Abdu et al., 2008), especially at altitudes of ∼280 km and below, and the occurrence of the largest electron density perturbations at the longer periods. These data suggest GW motions yielding electron density perturbations as large as ∼10 to 40% (Abdu et al., 2008; F08b) at altitudes from ∼200 to as high as ∼400 km, with implied neutral density and horizontal and vertical wind perturbations of ∼5 to 20% and ∼30 to 100 and ∼20 to $40\,\mathrm{m\,s}^{-1}$, respectively, for GWs with lower intrinsic frequencies of $\omega \sim N/5$ to $N/10$. These are consistent with the large oscillations at the bottomside F layer observed by Kelley et al. (1981) and Nicolls and Kelley (2005), but with the same caveats noted above concerning plasma processes that may cause over-estimates of neutral motions. Implied GW amplitudes at the higher frequencies within the observed range are correspondingly smaller, perhaps of order $u'_h \sim 10$ to $50\,\mathrm{m\,s}^{-1}$ and $w' \sim 5$ to $30\,\mathrm{m\,s}^{-1}$ at higher intrinsic frequencies of $\omega \sim N/2$. Of these GW perturbations, those at larger amplitudes and lower frequencies appear to have the greatest potential for influencing plasma processes during these times. We note, however, that the digisonde temporal resolution is sufficiently coarse to potentially prevent sensitivity to the higher-frequency motions anticipated at these altitudes by FV08, thus potentially underestimating both the amplitudes and the potential effects of such motions if these estimates are accurate. We also note that downward phase progression

of the electron density perturbations, while clear indicators of GW influences, are not required features of GW responses, as apparently vertical phase structures are also expected to accompany GWs near their turning levels at the highest altitudes (see Sects. 2.2.3 and 3.2.3).

Other evidence of GWs at the bottomside F layer and above is obtained from GPS estimates of total electron content (TEC) and its temporal derivative, which are assumed to be weighted towards the altitude of maximum electron density, typically ∼300 km. GW zonal and vertical winds in the equatorial F layer are expected to cause polarization electric fields in the presence of non-conducting E layers under typical nighttime conditions which could result in F-layer height oscillations with corresponding modulations in TEC. Similarly, GW meridional winds that yield undetectable responses very close to the dip equator will yield F-layer height modulations with increasing magnetic field inclination away from the dip equator which could also result in corresponding modulations in TEC. In each case, vertical displacements of the F-layer plasma are expected to result in modulated recombination loss and the associated TEC value.

Examples of $d$(TEC)/dt estimates derived from GPS data obtained at Fortaleza on 24 October for a number of satellite overpasses are shown in Fig. 7 of F08a. These suggest typical GW periods at these altitudes of ∼15 to 30 min, with suggestions of somewhat longer periods as well on occasion. The various satellites viewed by the receivers during these times yield similar temporal variations at the same times, suggesting spatial coherence among the various "piercing points" of the ionosphere. These data are challenging to interpret unambiguously, however, because it is difficult to separate temporal variations that may be due to GW propagation from possible spatial variations accompanying slow satellite motion. The apparent spatial and/or temporal variability could also arise from plasma bubbles themselves following their generation at the bottomside F layer. But this cannot explain the variability at earlier times (prior to ∼21:20 UT) that is almost certainly a signature of GWs in the neutral thermosphere (Swartz and Woodman, 1998). Thus, the TEC variability provides compelling evidence of GW perturbations at F-layer altitudes occurring at periods consistent with the expectations of theory for GWs arising from convective sources at lower altitudes.

Additional insights into possible GW perturbations of the neutral thermosphere come from 1356 Å emissions observed with cross-track scans by the TIMED/GUVI instrument. The descending node of each TIMED orbit provides two views of the plasma depletions having a component normal to the magnetic field from which tomographic retrievals of electron densities may be performed (Kamalabadi et al., 1999, 2002; Comberiate et al., 2007). The major assumption was that electron density fluctuations were approximately constant along magnetic field lines. The inversion method, the derived electron densities, and comparisons with images of the same plasma depletions seen from the ground in 6300 Å emissions are discussed in this special issue by Kamalabadi et al. (2008). Here we are interested primarily in the ability to infer electron density variations extending down to ∼100 km altitude with horizontal and vertical resolution of ∼40 and 20 km, respectively. Examples of these images are shown for two longitude bands spanning ∼36° to 46° W and ∼57° to 67° W over eastern and west-central Brazil on 1 October (day 274) in Fig. 4. Inspection reveals significant depletions in electron density extending upward from ∼100 km and having E-W scales of ∼200 to 500 km and above. Importantly, we note that large fractional perturbations extend to the lowest altitudes, and specifically below ∼250 km where digisonde data were sparse. Electron density fluctuations at these altitudes appear to be comparable to, or larger than, those observed in digisonde data discussed above. Electron density fluctuations at these altitudes may be either field-aligned extensions of plasma bubbles at higher altitudes at the dip equator or electron density responses to neutral motions, though again with the same caveats about inferred amplitudes. But if so, and using Eqs. (8) to (10), we infer possible neutral density and horizontal wind fluctuations of ∼10 to 20% and ∼40 to 80 ms$^{-1}$, respectively, as above. Intrinsic frequencies could be guessed crudely from the slopes of the depletions, but are most likely to be $\omega \sim N/3$ or higher at the highest altitudes.

### 2.2.3 Implications of GW propagation theory for GW parameters

FV08 employed ray tracing methods to show how GWs propagating into the thermosphere from sources in the lower atmosphere will be influenced by varying thermospheric temperatures and winds. A number of influences on GW propagation were found to be important, among them 1) refraction to smaller vertical wavelengths that enhanced their dissipation at lower altitudes, 2) refraction to larger vertical wavelengths that either contributed to reflection at turning levels or enabled much higher penetration into the thermosphere, and 3) elevated thermospheric densities at higher temperatures that decreased kinematic viscosity and thermal diffusivity and enhanced vertical penetration. The combined effects of these various influences led to removal of the majority of GW horizontal wavelengths and all but the highest GW frequencies able to propagate vertically at the highest altitudes. Those GWs that are found to penetrate to the highest altitudes are in all cases the GWs that are Doppler shifted to higher intrinsic frequencies (up-shifted GWs with smaller intrinsic than observed periods) and avoid encountering turning levels. Up-shifted GWs typically penetrate ∼50 and 100 km higher than unshifted and down-shifted GWs, respectively, for moderate Doppler shifting, and they have larger horizontal and vertical wavelengths at the highest altitudes. These effects are accentuated further for stronger Doppler shifting (∼200 ms$^{-1}$), with differences in penetration altitudes as high as ∼150 to 200 km at even larger horizontal and vertical

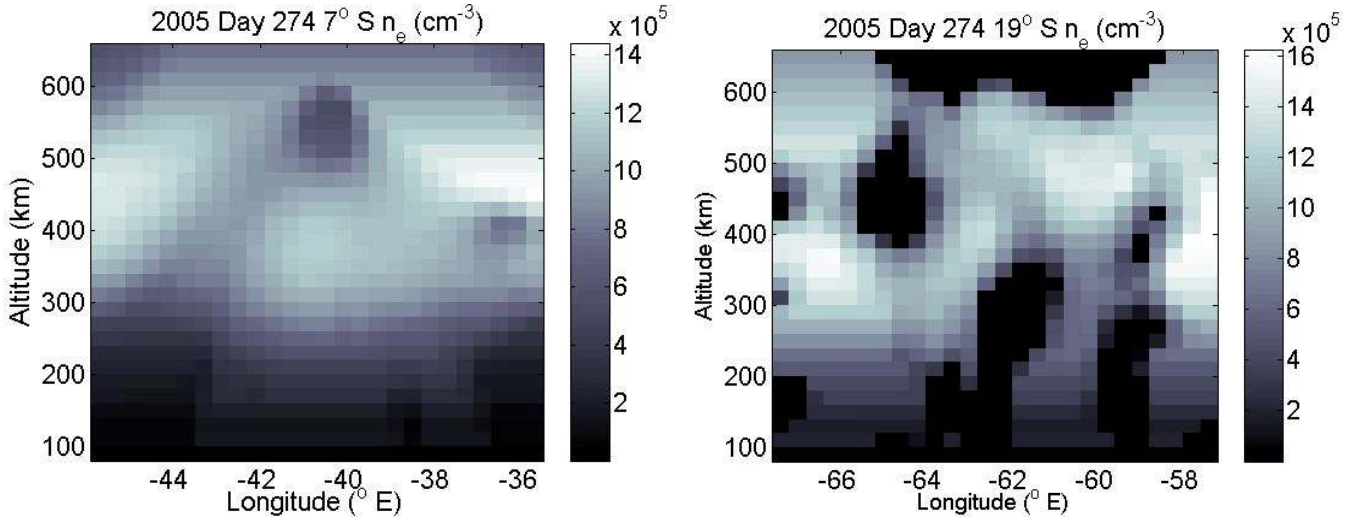


**Fig. 4.** Vertical cross-sections of electron densities indicative of plasma depletions at 7° S and 19° S (left and right) and spanning latitudes of ∼36° to 46° W and ∼57° to 67° W, respectively, from tomographic inversions of GUVI 1356 Å emissions on successive TIMED orbits over Brazil on 1 October 2005 (day 274). The tomographic inversions enabled horizontal and vertical resolution of 40 and 20 km, respectively. Note the very different spatial structures at the ∼100-min TIMED orbital sampling interval.

wavelengths for thermospheric temperatures occurring during SpreadFEx. Thus, while it is possible for GWs having a range of wavelengths, periods (observed or intrinsic), and propagation directions to reach bottomside F-layer altitudes, the GWs arising in the lower atmosphere that almost certainly make the dominant contributions to density and velocity perturbations at the highest altitudes will be the up-shifted GWs whenever significant mean winds are present in the MLT. Given the ubiquitous nature and presence of tidal motions at these altitudes, this would appear to be the case essentially all of the time. In terms of influences on plasma instability seeding processes, however, we also must consider the orientation of the GWs that reach the bottomside F layer, as this will vary with tidal winds, in time, altitude, and latitude. GW orientation will also be a major factor in determining field-line-integrated effects and correlations between differing influences on various terms in plasma instability growth rates, whether they occur on, or at some distance from, the dip equator.

Decreasing neutral density with altitude obviously allows enormous GW amplitude growth into the thermosphere. Mean density decreases by $\sim 10^{11}$ from the ground to ∼250, 300, and 350 km, respectively, for minimum, mean, and maximum solar forcing and thermospheric temperatures. This implies comparable GW amplitude growth at these altitudes for the different thermospheric temperatures, apart from the effects of GW dispersion with altitude. Assuming, for illustration, that GWs propagate without dissipation from the MLT so that total momentum flux is conserved, but that it is distributed over an area that increases as $z^2$, we can estimate the amplitude growth with altitude for each thermospheric temperature. These results are shown at 50-km intervals in Table 1 up to the highest altitudes to which up-shifted GWs can penetrate for a mean wind of 100 $\mathrm{ms}^{-1}$. In each case, we have estimated the increase in GW horizontal perturbation velocity relative to its value at 80 km. The growth with altitude is of course much more rapid for a thermospheric temperature of 600 K because of the much more rapid decay of density with altitude in this case. As we should expect, the amplification factors are approximately the same at the same density for each temperature profile, with the differences due to the greater GW dispersion at higher altitudes for the higher thermospheric temperatures.

The results discussed above imply potentially large GW amplitudes and effects on neutral and plasma processes at the bottomside F layer if they are efficiently excited at lower altitudes and reach the thermosphere relatively unattenuated. To explore this more fully, we display in Table 2 the highest altitudes achieved for GWs with surviving momentum fluxes of ∼50% and ∼3%, the approximate range of horizontal wavelengths that reach these altitudes, and the GW horizontal velocity perturbations at these altitudes, relative to the nominal value of $u'_h$ ∼1 $\mathrm{ms}^{-1}$ at 80 km for each of the Doppler-shifting environments considered by FV08 (up-shifted, unshifted, and down-shifted in a lower thermospheric zonal wind of 100 $\mathrm{ms}^{-1}$). Similar results for GWs up-shifted and down-shifted by a thermospheric wind of 200 $\mathrm{ms}^{-1}$ are shown in Table 3. As discussed by FV08, the up-shifted GWs clearly attain the highest altitudes for all solar conditions. The highest altitudes for all Doppler-shifting conditions and the largest differences in penetration altitudes also occur for maximum thermospheric temperatures. This

**Table 1.** Approximate variations with altitude of the area over which momentum fluxes for a specific GW are distributed, $A(z)$, mean density, $\rho(z)$, and implied GW horizontal perturbation velocity for thermospheric temperatures of 600, 1000, and 1600 K. We have assumed no dissipation for the estimates in this table, and no data are provided for altitudes above those to which GWs are expected to penetrate.

| Height, | Area factor | $T$=600 K | | $T$ =1000 K | | $T$=1600 K | |
|---|---|---|---|---|---|---|---|
| $z(km)$ | $A(z)$ | $\rho$ (g/m$^3$) | $u'_h/u'_{h80}$ | $\rho$ (g/m$^3$) | $u'_h/u'_{h80}$ | $\rho$ (g/m$^3$) | $u'_h/u'_{h80}$ |
| 400 | ∼31 | – | – | – | – | $\sim 3\times10^{-9}$ | ∼300 |
| 350 | ∼24 | – | – | $\sim 2\times10^{-9}$ | ∼500 | $\sim 10^{-8}$ | ∼200 |
| 300 | ∼17 | $\sim 5\times10^{-10}$ | ∼1000 | $\sim 10^{-8}$ | ∼250 | $\sim 3\times10^{-8}$ | ∼120 |
| 250 | ∼12 | $\sim 7\times10^{-9}$ | ∼350 | $\sim 7\times10^{-8}$ | ∼100 | $\sim 10^{-7}$ | ∼80 |
| 200 | ∼7 | $\sim 10^{-7}$ | ∼120 | $\sim 5\times10^{-7}$ | ∼50 | $\sim 5\times10^{-7}$ | ∼50 |
| 80 | 1 | $\sim 10^{-2}$ | 1 | $\sim 10^{-2}$ | 1 | $\sim 10^{-2}$ | 1 |

**Table 2.** Approximate maximum penetration altitude, the range of GW horizontal wavelengths that reach these altitudes, and the amplification factor for GW horizontal velocities at this altitude (AF=$u'_h/u'_{h80}$) for thermospheric temperatures of 600, 1000, and 1600 K (top to bottom), up-shifted, unshifted, and down-shifted GWs (left to right) assuming a zonal wind in the thermosphere of 100 ms$^{-1}$, and surviving momentum flux fractions of 50% and 3%.

| Dopp.Sh. | up-sh, 50% | up-sh, 3% | un-sh, 50% | un-sh, 3% | dn-sh, 50% | dn-sh, 3% |
|---|---|---|---|---|---|---|
| 600 K | ∼240 km | ∼260 km | ∼220 km | ∼240 km | ∼180 km | ∼200 km |
| ($z$, $\lambda_h$, AF) | ∼150−300 | ∼150−250 | ∼150−250 | ∼150−250 | ∼150−300 | ∼150−300 |
| | ∼200 | ∼80 | ∼120 | ∼40 | ∼60 | ∼20 |
| 1000 K | ∼290 km | ∼330 km | ∼240 km | ∼290 km | ∼190 km | ∼230 km |
| ($z$, $\lambda_h$, AF) | ∼200−400 | ∼200−300 | ∼150−350 | ∼150−350 | ∼150−500 | ∼150−350 |
| | ∼150 | ∼60 | ∼70 | ∼30 | ∼30 | ∼15 |
| 1600 K | ∼310 km | ∼390 km | ∼250 km | ∼330 km | ∼190 km | ∼230 km |
| ($z$, $\lambda_h$, AF) | ∼200−500 | ∼250−350 | ∼150−350 | ∼200−350 | ∼150−350 | ∼150−350 |
| | ∼100 | ∼40 | ∼60 | ∼20 | ∼30 | ∼10 |

is despite significantly greater reflection at turning levels of the up-shifted higher-frequency GWs at smaller horizontal wavelengths as thermospheric temperatures and winds increase.

Summarizing the theoretical studies, up-shifted GWs that escape reflection at turning levels have the greatest potential to reach the bottomside F layer with the largest amplitudes, momentum fluxes, and implied body forces because they are refracted to higher intrinsic frequencies and larger vertical wavelengths that enhance vertical group velocity and lessen viscous dissipation. Unshifted GWs nevertheless can also penetrate to almost the same altitudes, and with amplitudes and momentum fluxes that are nearly as large. GW density and horizontal velocity perturbations can reach ∼100 times or more their magnitudes at 80 km. Horizontal wavelengths expected to achieve the highest altitudes vary with the degree of Doppler shifting, but are in the range ∼150 to 350 km for the solar conditions and thermospheric temperature representative of SpreadFEx measurements. The spatial and temporal scales of the GWs expected theoretically to penetrate from sources in the lower atmosphere into the thermosphere agree reasonably well with previous measurements and those performed during SpreadFEx. Specific GW perturbations at the bottomside F layer inferred from SpreadFEx neutral and electron density measurements and viscous GW theory are assessed below. A summary of these expected perturbations for mean solar conditions, an intermediate electron/neutral perturbation density ratio of $(\rho'_e/\rho_e)/(\rho'/\rho)\sim4$ (from Eq. 8), and the various wind profiles considered representative is provided in Table 4.

## 3 Impacts of GWs and tides on plasma instability parameters

SpreadFEx data and ray tracing studies of GW propagation, refraction, and dissipation reviewed above have provided specific guidance on those GW amplitudes, horizontal and vertical wavelengths, and observed and intrinsic periods expected to achieve significant amplitudes at the bottomside F layer. Theory suggests that horizontal and vertical

**Table 3.** As in Table 2, but only for up-shifted and down-shifted GWs for a zonal wind in the thermosphere of 200 $ms^{-1}$.

| Dopp.Sh. | up-sh, 50% | up-sh, 3% | dn-sh, 50% | dn-sh, 3% |
|---|---|---|---|---|
| 600 K ($z$, $\lambda_h$, AF) | ∼250 km | ∼270 km | ∼160 km | ∼170 km |
| | ∼200−600 | ∼200−300 | ∼150−350 | ∼100−600 |
| | ∼200 | ∼80 | ∼60 | ∼20 |
| 1000 K ($z$, $\lambda_h$, AF) | ∼300 km | ∼350 km | ∼160 km | ∼170 km |
| | ∼250−600 | ∼250−350 | ∼100−600 | ∼100−600 |
| | ∼150 | ∼60 | ∼30 | ∼15 |
| 1600 K ($z$, $\lambda_h$, AF) | ∼350 km | ∼400 km | ∼160 km | ∼170 km |
| | ∼300−600 | ∼250−600 | ∼150−600 | ∼100−800 |
| | ∼100 | ∼40 | ∼30 | ∼10 |

**Table 4.** Approximate GW horizontal velocity, neutral and electron density perturbations, and horizontal wavelength ranges for mean solar conditions, $(\rho'_e/\rho_e)/(\rho'/\rho)$∼4, and unshifted (left column), up-shifted with a 100 $ms^{-1}$ mean wind (center column), and up-shifted with a 200 $ms^{-1}$ mean wind (right column). All values are based on the nominal GW amplitude of 1 $ms^{-1}$ at 80 km. Note that the up-shifted GWs that propagate to the highest altitudes for a mean wind of 200 $ms^{-1}$ occur for larger horizontal wavelengths and lower initial GW frequencies.

| $z$ (km) | parameter | unshifted | up-shifted (100 $ms^{-1}$) | up-shifted (200 $ms^{-1}$) |
|---|---|---|---|---|
| 200 | $u'_h$ | ∼50 $ms^{-1}$ | ∼50 $ms^{-1}$ | ∼50 $ms^{-1}$ |
| | $\rho'/\rho$ | ∼5−10% | ∼5−10% | ∼5−10% |
| | $\rho'_e/\rho_e$ | ∼20−40% | ∼20−40% | ∼20−40% |
| | $\lambda_h$ | ∼100−600 km | ∼100−1000 km | ∼150−1000 km |
| 250 | $u'_h$ | ∼50 $ms^{-1}$ | ∼100 $ms^{-1}$ | ∼100 $ms^{-1}$ |
| | $\rho'/\rho$ | ∼5−10% | ∼10−20% | ∼10−20% |
| | $\rho'_e/\rho_e$ | ∼20−40% | ∼40−80% | ∼40−80% |
| | $\lambda_h$ | ∼150−200 km | ∼150−600 km | ∼200−1000 km |
| 300 | $u'_h$ | ∼10 $ms^{-1}$ | ∼100 $ms^{-1}$ | ∼150 $ms^{-1}$ |
| | $\rho'/\rho$ | ∼1−2% | ∼10−20% | ∼15−30% |
| | $\rho'_e/\rho_e$ | ∼5−10% | ∼40−80% | ∼60−100% |
| | $\lambda_h$ | ∼150−200 km | ∼200−300 km | ∼250−600 km |
| 350 | $u'_h$ | – | ∼10 $ms^{-1}$ | ∼100 $ms^{-1}$ |
| | $\rho'/\rho$ | – | ∼1−2% | ∼10−20% |
| | $\rho'_e/\rho_e$ | – | ∼4−8% | ∼40−80% |
| | $\lambda_h$ | – | ∼200 km | ∼250−350 km |

wavelengths of ∼150 to 400 km and observed periods of ∼10 to 30 min will be most common, at least if GWs from lower atmospheric sources dominate. Corresponding intrinsic periods are expected to be somewhat shorter because of the preferential penetration to high altitudes of up-shifted GWs. SpreadFEx measurements, and previous studies of GWs in the TI, are largely consistent with these expectations. There is also evidence in some data, however, of even longer observed periods, larger spatial scales, and higher penetration altitudes. These suggest either 1) even greater Doppler shifting by stronger winds in the MLT or 2) additional sources of GWs having larger scales and higher phase speeds at higher altitudes. Of these GWs, we can most easily estimate the effects of those for which SpreadFEx data and theory provide specific guidance. We can, however, guess at the relative amplitudes and effects of larger-scale GWs from other sources in cases where we have evidence of GWs from both sources present in the same data.

### 3.1 Estimates of GW perturbations at the bottomside F-layer

For GWs that arise from convection, we can extrapolate, as outlined above, from the 2-D wavenumber spectrum scaled

to fit SpreadFEx airglow measurements and shown in Fig. 2. From this spectrum, we infer maximum GW horizontal velocity perturbations of $\sim$1 ms$^{-1}$ at horizontal wavelengths of 200 to 300 km for an initial frequency $\omega$=$N$/2, mean solar conditions, and an 80-km altitude. Corresponding horizontal velocity perturbations at $\sim$290 and 240 km for upshifted and unshifted GWs, respectively, with a mean wind of 100 ms$^{-1}$ are $\sim$150 and 70 ms$^{-1}$, with expected neutral and plasma density perturbations given by Eqs. (5) and (7). The same velocity perturbations also are expected for a wind of 200 ms$^{-1}$, but at slightly higher altitudes and horizontal wavelengths. Vertical displacements accompanying these perturbations are likewise large; GW perturbations decrease in amplitude at higher altitudes, but are still $\sim$20% as large at $\sim$50 km higher. These estimates are summarized in Tables 2 and 3 for easy reference in our discussion below. The result of this assessment is that GW perturbations to neutral winds and neutral and plasma densities arising due to deep convection have the potential to be significant (i.e. significant fractions of mean quantities) at potential plasma instability seeding altitudes of $\sim$250 to 300 km.

### 3.2 GW and tidal impacts on plasma instability parameters

We reviewed above the observational and theoretical evidence for GW propagation to high altitudes, the GW spatial and temporal scales that reach the highest altitudes, and the GW amplitudes that may be expected at the bottomside F layer based on measurements and analyses performed as part of SpreadFEx. Implicit in this assessment was an awareness of the presence of large-amplitude tidal motions in the lower thermosphere, which appear to contribute the majority of the large-scale wind shear in the MLT accounting for GW refraction and filtering as well as the wind field extending to the bottomside F layer and above. Indeed, it was argued in our initial SpreadFEx overview by F08b that the tidal motions themselves may play a central role in preconditioning the bottomside F layer for plasma instabilities potentially triggered by GW perturbations occurring at smaller spatial scales. Here, we estimate the likely influences of both tidal and GW wind and temperature (or density) perturbations at the bottomside F layer on the neutral and plasma quantities that play a role in defining plasma instability growth rates and potential triggering of plasma bubbles penetrating to much higher altitudes. We also consider how GWs occurring at $\sim$10° off the dip equator at somewhat lower altitudes might contribute to modulation of plasma instability growth rates through field line-integrated effects.

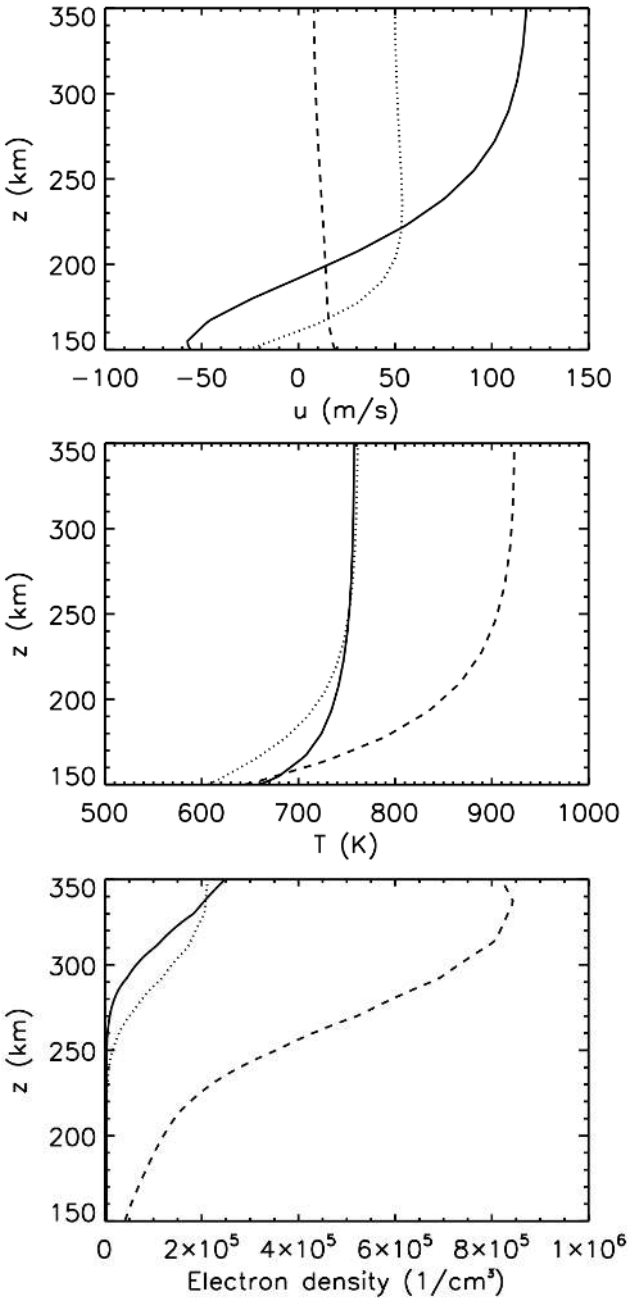


**Fig. 5.** Zonal wind, temperature, and electron density variations in the thermosphere on 25/26 October 2005 at 50° W, 12.5° S over Brazil at 21:00 (dashed), 00:00 (solid), and 03:00 UT (dash-dotted) from a TIME GCM simulation spanning the SpreadFEx campaign period and initialized with the global NCEP reanalysis for this period.

#### 3.2.1 Tidal structures and influences

The diurnal and semidiurnal tides are believed to comprise the dominant neutral motion field at F-layer altitudes (though PW periods also map to higher altitudes), and their temporal behavior appears to have a potential to make clear contributions to plasma instability processes at the bottomside F layer, based on the NCAR thermosphere-ionosphere-mesosphere-electrodynamics (TIME) general circulation model (GCM) description of these structures at equatorial latitudes (F08b). Tidal theory and viscous dissipation

suggest that the migrating tides have vertical wavelengths of ∼25 km or larger in the MLT, with the tidal wind fields becoming more nearly uniform with altitude above ∼250 km due to increasing in situ forcing with altitude. Examples of the tidal influences on the wind, temperature, and electron density fields at higher altitudes on the dip equator on 25/26 October 2005 from a TIME GCM simulation initialized with NCEP reanalysis data for this interval are shown in Fig. 5. These fields indicate significant oscillations and gradients at MLT altitudes, with increasing vertical wavelengths, decreasing gradients, but larger amplitudes as altitudes increase. Note that the TIME GCM tidal structures at F-layer altitudes have yet to be validated, so their detailed amplitude and phase structures should be considered to be only suggestive at this time. They are suggestive, however, of the temporal behavior of the neutral wind perturbations that potentially contribute to plasma drifts, plasma density perturbations, and their gradients at F-layer altitudes, and we consider them a sufficiently good approximation for our purposes here. In particular, TIME GCM winds become eastward at about the time of plasma bubble onset, though this transition is seen to vary from day to day. Tidal amplitudes in the TIME GCM simulation are also variable from day to day, but appear to validate our use of thermospheric winds of ∼100 to 200 $ms^{-1}$ for purposes of computing GW refraction and thermospheric penetration by FV08. Indeed, we will argue here that temporally-variable tidal amplitudes, due either to variable forcing in the lower atmosphere or upward mapping of tidal and PW features from below, should be expected to contribute significantly to ESF and plasma bubble occurrence modulation and statistics at F layer and higher altitudes. A similar suggestion was made based on 6300 Å Fabry Perot interferometer wind measurements in Peru (Meriwether et al., 2008).

We first examine the implications of the TIME GCM simulation constrained by NCEP reanalysis data for tidal winds and temperatures (or densities) around the time of plasma bubble seeding to assess its potential direct contributions to the dynamics and parameters influencing plasma growth rates. We will then examine the likely GW influences within this assumed tidal environment. The zonal wind, temperature, and electron density profiles shown in Fig. 5 are used for this purpose. This date was chosen as it exhibited one of the more dynamically active intervals at the bottomside F layer, with significant vertical plasma motions at several periods that appeared to be correlated with plasma bubbles extending to high altitudes (Abdu et al., 2008; Haase et al., 2008; Takahashi et al., 2008). We note, however, that while the TIME GCM winds may be representative of TI tidal structure in general, they are almost surely not an accurate local prediction of the specific tidal motions occurring on this day. Nevertheless, these profiles suggest that zonal winds are generally weak at ∼21:00 UT and before, but swing strongly positive (eastward) thereafter at F-layer altitudes, which appears to correlate well with onset times for plasma bubbles noted by previous authors (Swartz and Woodman, 1998). A significant eastward wind shear $\partial U_{\rm tide}/\partial z \sim 0.002\,s^{-1}$ accompanies this tidal structure, propagates downward with time, and yields a zonal wind difference of ∼150 $ms^{-1}$ between altitudes of ∼150 to 250 km, though tidal amplitudes, gradients, and timing will vary day-to-day. Indeed, both the tendency for eastward motions beginning shortly after 00:00 UT (21:00 LT) and the strong wind shear at lower altitudes appear to play a role in the plasma instability growth rate estimates discussed by Hysell and Kudeki (2004), Kudeki et al. (2007), and others, and assessed employing our current results by Abdu et al. (2008) and Kherani et al. (2008) in this issue.

At higher altitudes, the neutrals and plasma are closely coupled, so the tidal winds are expected to cause an increasing eastward plasma drift (in both time and altitude) accompanying the descending phase of the tidal wind field. At lower altitudes, the neutrals and plasma are not as tightly coupled, so we expect a westward plasma drift relative to the westward (or weaker eastward) neutral wind during early evening hours. This scenario is depicted in the left side of each panel of Fig. 6. The result of these large-scale dynamics is a neutral and plasma flow structure that has several elements that potentially contribute to plasma growth rates discussed by various authors. These are 1) a significant eastward neutral wind at bottomside F layer and higher altitudes, 2) a significant difference between neutral motions and plasma drifts, and 3) enhanced neutral and plasma density gradients that are directly correlated with the eastward tidal wind. Nominal tidal amplitudes, their implications for other quantities, and the phase relations among them are listed for convenience in the upper portion of Table 5. Vertical tidal motions are expected to be small and likely do not contribute as much to potential plasma instability processes as the vertical neutral motions accompanying the GWs reaching these altitudes.

We also expect tidal effects on plasma densities and plasma gradients that may reach significant magnitudes and impact plasma instability growth rates. In particular, an eastward tidal wind accompanies enhanced potential temperature (or density) gradients, implying a positive correlation between eastward winds (which enhance $(U_{\rm tide}-U_{pl})$) and enhanced electron density gradients, both of which enhance plasma instability growth rates according to the theory by Kudeki et al. (2007). The magnitude of this enhancement can be estimated from the fractional tidal temperature perturbations $T'/T$, the tidal vertical wavelength, estimated as $\lambda_z \sim 2\pi U_{\rm tide}/(\partial U_{\rm tide}/\partial z) \sim 300$ km, yielding fractional electron density gradients comparable to, or larger than, fractional electron densities (see Eqs. 12 and 16 below). Other fields dependent on coupling between neutrals and the plasma, such as polarization electric fields, are assessed by Abdu et al. (2008) and Kherani et al. (2008).

**Table 5.** Tidal and GW perturbations from the TIME GCM and GW theory, respectively, at the bottomside F layer with our assumptions of tidal and GW vertical wavelengths (∼300 and 150 km, respectively), GW intrinsic frequency ($\omega_I \sim N/2$), and tidal and GW amplitudes (at top). Phase correlations show lags relative to the eastward tidal wind and GW horizontal wind in the direction of propagation (westward), $U_{\rm tide}$ and $u'_h$, respectively. Estimates for ($U_{\rm tide}$–$U_{pl}$) are at lower altitudes where the neutrals and plasma are not strongly coupled. Tidal effects on electron densities are nominal, as they are difficult to distinguish from LT effects in the TIME GCM results.

| tidal amplitude (right) tidal/GW parameters | | phase correl. with $U_n$ or $u'_h$ | $U_n \sim 100\,{\rm ms}^{-1}$ $u'_h \sim 50\,{\rm ms}^{-1}$ | $U_n \sim 200\,{\rm ms}^{-1}$ $u'_h \sim 100\,{\rm ms}^{-1}$ |
|---|---|---|---|---|
| Tidal | ($U_{\rm tide}$–$U_{pl}$) | – | $\sim 150\,{\rm ms}^{-1}$ | $\sim 250\,{\rm ms}^{-1}$ |
| fields | $T'$ (or $\theta'$) | ∼90° | ∼100 K | ∼200 K |
| | $T'/T$ ($\theta'/\theta$) | ∼90° | ∼5−10% | ∼10−20% |
| | $\rho'/\rho_0$ | ∼270°(∼−90°) | ∼5−10% | ∼10−20% |
| | $\rho'_e/\rho_e$ | ∼270° | ∼10−20% | ∼20−40% |
| | $(H_e/\rho_e)\partial\rho'_e/\partial z$ | ∼0° | ∼10−20% | ∼20−40% |
| GW r | $u'_h$ | – | $\sim 50\,{\rm ms}^{-1}$ | $\sim 100\,{\rm ms}^{-1}$ |
| fields | $w'$ | ∼0° | $\sim 30\,{\rm ms}^{-1}$ | $\sim 60\,{\rm ms}^{-1}$ |
| | $T'$ (or $\theta'$) | ∼270° (∼−90°) | ∼50−100 K | ∼100−200 K |
| | $T'/T$ ($\theta'/\theta$) | ∼270° | ∼5−10% | ∼10−20% |
| | $\rho'/\rho$ | ∼90° | ∼5−10% | ∼10−20% |
| | $\rho'_e/\rho_e$ | ∼90° | ∼20−40% | ∼40−80% |
| | $(H_e/\rho_e)\partial\rho'_e/\partial z$ | ∼180° | ∼80−100% | ∼100% |

### 3.2.2 GW structures and influences

Potential GW influences on ESF and plasma bubble seeding have been studied for almost four decades, both theoretically (Whitehead, 1971; Beer, 1973; Klostermeyer, 1978) and observationally (e.g. McClure et al., 1998). Early studies that considered relatively small GW amplitudes judged these influences to be insufficient to seed plasma bubbles, while other observational studies suggested that GWs having larger amplitudes could contribute effectively (Kelley et al., 1981; Kelley, 1989; Hysell et al., 1990). Later numerical studies also exhibited bubble seeding for a variety of initial conditions (Huang et al., 1993; Huang and Kelley, 1996a, b, c; Sekar and Kelley, 1998). Other efforts examined the GW characteristics and orientations most conducive to potential seeding conditions (Prakash and Pandey, 1985; Kelley, 1989). Despite these efforts, there remains no consensus on the role of GWs in seeding plasma bubbles or the specific mechanisms by which this might occur to date.

We consider here the GW orientations and structures implied by our SpreadFEx measurements and theoretical efforts and their possible contributions to factors influencing plasma instability growth rates. Our SpreadFEx observations, ray tracing studies of GWs arising from convective plumes (V08a), the more general assessment of GW penetration into the thermosphere for various mean wind and solar forcing conditions (FV08), and TIME GCM tidal winds (and the associated GW filtering) imply a strong preference for westward GW propagation, both in the MLT and at the bottomside F layer at times relevant to plasma bubble seeding. Specifically, the GWs that can apparently reach the highest altitudes are up-shifted by eastward MLT and TI tidal winds, implying that only those GWs having largely westward propagation can easily reach bottomside F-layer altitudes and influence plasma instability processes.

To evaluate potential GW contributions to plasma instability growth rates, we must estimate both the perturbation wind fields and the plasma densities and plasma density gradients that accompany the GWs penetrating to bottomside F-layer altitudes. The phase relations between the GW horizontal and vertical perturbation velocities and neutral and electron density perturbations are given by Eqs. (4) to (7) above. To estimate electron density gradients, we assume that $|\rho'_e/\rho_e|$ varies slowly with altitude, based on the $\rho'_e/\rho_e$ estimates obtained from the São Luis digisonde and the GUVI tomographic electron density images shown in Figs. 3 and 4. With this approximation, $|\rho'_e| \sim \exp(z/H_e)$ and the total electron density gradient is

$$\begin{aligned} \partial\rho_e/\partial z &= \rho_e/H_e + \partial/\partial z(|\rho'_e|e^{imz}) \\ &= \rho_e[1/H_e + (\rho'_e/\rho_e)(1/H_e + im)], \end{aligned} \tag{11}$$

where the last term expresses the variation with GW phase and altitude prior to significant viscous dissipation. Then the ratio of perturbation to mean electron density gradients is

$$(\partial\rho'_e/\partial z)/(\partial\rho_e/\partial z) \sim (1 + imH_e)(\rho'_e/\rho_e), \tag{12}$$

which varies with the GW phase with a maximum enhancement, relative to the fractional electron density, of $(1+mH_e)=(1+2\pi H_e/\lambda_z)$ which may exceed a factor of 2 for $\lambda_z < 2\pi H_e$., for $\lambda_z \sim 200$ km and $H_e \sim 30$ km. For larger

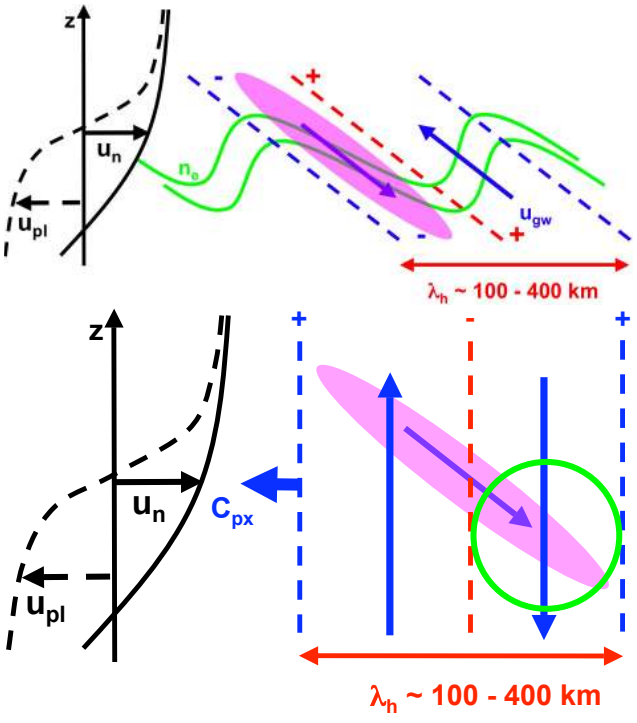


**Fig. 6.** Profiles of neutral wind ($U_n$, solid black line) and plasma motion ($U_{pl}$, dashed black line) at the bottomside F layer (left) along the dip equator expected under ESF and RTI seeding conditions. At top right are shown surfaces of constant electron density (green) due to an upward- and westward-propagating GW. Maximum upward and downward displacements are shown with blue and red dashed lines, respectively, GW neutral velocities are shown with blue arrows, and the region with the maximum electron density gradient is shown in pink. At bottom right are shown the region of enhanced electron density accompanying the GW propagating upward and westward and the corresponding maximum displacements and neutral velocities for a GW that is close to a turning level at which $\lambda_z => \infty$ and $w' \gg u'_h$. Note that a GW near a turning level may further enhance downward (or upward) motions without significantly impacting neutral or electron density gradients.

$H_e \sim 100$ km or smaller $\lambda_z$, fractional electron density gradients may exceed fractional electron densities by factors of ~2 to 5 for mean solar conditions, and we will assume a factor of 3 for our discussion below.

The GW structure and the correlations among fields for a westward-propagating GW are shown at the right side of the upper panel of Fig. 6. Specifically, a westward-propagating GW yields a positive correlation between eastward wind perturbations and plasma density gradients, both of which are expected to enhance plasma instabilities described by Hysell et al. (2004) and Kudeki et al. (2007). The GW vertical velocity is anti-correlated with the eastward GW wind perturbation and enhanced gradients of neutrals and electron densities. It is thus downward where the eastward GW wind and enhanced plasma gradients may enhance the plasma growth rates, and is also beneficial for plasma instabilities, especially the RTI (Fejer, 1996).

We reviewed in Sect. 2 SpreadFEx and related evidence for GW scales and amplitudes in the neutral atmosphere and at the bottomside F layer. Both observations and theory helped to constrain estimates of various GW parameters that may influence plasma instability growth rates, and we summarize and discuss these results here. The theoretical study by FV08 provided strong constraints on GW propagation direction and spatial and temporal scales in the lower thermosphere. This led to the requirement of westward propagation in eastward tidal winds noted above. Spatial scales at higher altitudes are likewise constrained, with minimum horizontal and vertical wavelengths of ~100 km each and intrinsic frequencies of $\omega \sim N/3$ or higher. This theory also placed constraints on GW amplitudes, but only relative to their values at ~80 km. Fortunately, the values assumed at 80 km are consistent with the GW convective source spectra inferred from the reverse ray tracing of large-scale GWs observed in OH airglow by V08b and VF08.

Direct measurements of electron density perturbations at the bottomside F layer and below in the absence of plasma bubbles nevertheless provide more direct, though qualitative, constraints on GW scales and amplitudes. These are based on digisonde and GUVI estimates of electron density perturbations over significant altitude ranges, as low as ~100 km from GUVI tomographic inversions and down to ~200 to 250 km with digisonde electron density estimates. São Luis digisonde data yielded estimates of fractional electron density perturbations that may be attributed to GWs as large as $\rho'_e/\rho_e \sim 20$ to 40% (see Fig. 3 and Abdu et al., 2008). GUVI electron density cross sections (Fig. 4), on the other hand, suggest even larger perturbations about the mean extending to very low altitudes.. To place reasonable upper limits on the range of GW perturbations we will examine in detail, we assume peak fractional electron density perturbations of ~40 to 80% at the bottomside F layer based on GUVI plasma density measurements. These estimates correspond to horizontal velocity perturbations of 50 and 100 $ms^{-1}$ for representative scale heights of $H \sim 30$ km and $H_e \sim 50$ km for mean neutral and electron densities. The larger amplitudes likely represent upper limits due to our assumption of only advective influences on plasma perturbations above. The various GW parameters and their relative phases are listed for these GW wind amplitudes in the lower part of Table 5.

### 3.2.3 Superposed GW and tidal structures and influences

We assume that plasma instabilities depend on the total perturbation fields, summing both tidal and GW components. We also employ our notation above, with tidal eastward and vertical velocities of $U_{\rm tide}$ and ~0, GW westward and vertical velocities of $u'_h$ and $w'$, and plasma drifts and fractional electron density gradients as defined above. The parameters

**Table 6.** Estimated tidal and GW parameters at the bottomside F layer based on SpreadFEx measurements and associated modeling. The center row shows parameters assuming an eastward tidal motion and a single westward- and vertically-propagating GW in its upward phase. The bottom row assumes the same tidal motion, but now with a westward-propagating GW approaching a turning level, with $m$=>0, largely vertical motions (w' ∼50 or 100 ms$^{-1}$, $u'_h$∼0), and essentially no induced electron density gradients. The same GW imagined in the center row could also contribute to the electron density gradient in the bottom row without overcoming the enhanced vertical motion due to the GW approaching its turning level.

| Tidal E winds | $U_n$∼100 ms$^{-1}$ | $U_n$∼100 ms$^{-1}$ | $U_n$∼200 ms$^{-1}$ | $U_n$∼200 ms$^{-1}$ |
|---|---|---|---|---|
| GW $u'_h$, $w'$ (propagating) | $u'_h$∼50 ms$^{-1}$<br>$w'$ ∼30 ms$^{-1}$ | $u'_h$∼100 ms$^{-1}$<br>$w'$ ∼60 ms$^{-1}$ | $u'_h$∼50 ms$^{-1}$<br>$w'$ ∼30 ms$^{-1}$ | $u'_h$∼100 ms$^{-1}$<br>$w'$ ∼60 ms$^{-1}$ |
| $U_{\rm tide}-u'_h$ | ∼50 ms$^{-1}$ | ∼0 ms$^{-1}$ | ∼150 ms$^{-1}$ | ∼100 ms$^{-1}$ |
| $U_{\rm tide}-u'_h-U_{pl}$ | ∼100 ms$^{-1}$ | ∼50 ms$^{-1}$ | ∼200 ms$^{-1}$ | ∼150 ms$^{-1}$ |
| $(H_e/\rho_e)\partial\rho'_e/\partial z$ | ∼−40% | ∼−80% | ∼−40% | ∼−80% |
| GW $u'_h$, $w'$ (turning level) | $u'_h$ ∼0 ms$^{-1}$<br>$w'$ ∼50 ms$^{-1}$ | $u'_h$∼0 ms$^{-1}$<br>$w'$ ∼100 ms$^{-1}$ | $u'_h$ ∼0 ms$^{-1}$<br>$w'$ ∼50 ms$^{-1}$ | $u'_h$ ∼0 ms$^{-1}$<br>$w'$∼100 ms$^{-1}$ |
| $U_{\rm tide}-u'_h$ | ∼100 ms$^{-1}$ | ∼100 ms$^{-1}$ | ∼200 ms$^{-1}$ | ∼200 ms$^{-1}$ |
| $U_{\rm tide}-u'_h-U_{pl}$ | ∼150 ms$^{-1}$ | ∼150 ms$^{-1}$ | ∼250 ms$^{-1}$ | ∼250 ms$^{-1}$ |
| $W$ (=$w'$) | ∼50 ms$^{-1}$ | ∼100 ms$^{-1}$ | ∼50 ms$^{-1}$ | ∼100 ms$^{-1}$ |
| $(H_e/\rho_e)\partial\rho'_e/\partial z$ | ∼+20% | ∼+40% | ∼+20% | ∼+40% |

that appear to be most relevant to an assessment of plasma instability growth rates may be written as

$$U_n = U_{\rm tide} - u'_h, \tag{13}$$

$$U_n - U_{pl} = U_{\rm tide} - u'_h - U_{pl}, \tag{14}$$

$$W = W_{\rm tide} + w' \approx w', \tag{15}$$

and

$$(\partial\rho'_e/\partial z)/(\partial\rho_e/\partial z) = (H_e/\rho_e)\partial\rho'_e/\partial z$$
$$= (H_e/\rho_e)[(\partial\rho'_e/\partial z)_{\rm tide} + (\partial\rho'_e/\partial z)_{GW}], \tag{16}$$

where $U_n$ is the total neutral eastward wind, $U_n$–$U_{pl}$ is the difference between the neutral eastward wind and the westward plasma drift (assumed to be $U_{pl}$∼50 ms$^{-1}$), $W$ is the total neutral vertical velocity, and $(\partial\rho'_e/\partial z)/(\partial\rho_e/\partial z)$ is the fractional electron density gradient due to both tidal and GW motions.

The above perturbation quantities are listed for four combinations of assumed GW and nominal tidal parameters in the central rows of Table 6, assuming GWs propagating upward and westward (with downward and eastward winds expected to contribute to plasma instabilities). Examination reveals that all combinations of GW and tidal parameters yield enhanced contributions to plasma instabilities in the downward phase of the GW. In particular, eastward GW winds augment the eastward tidal winds anticipated from the TIME GCM in the early evening hours and contribute to enhanced plasma density gradients if the advective influences discussed above dominate possible chemical or electrodynamic effects. The case of larger tidal amplitudes and smaller GW amplitudes appears not to be as favorable to plasma instability because it reduces the plasma density gradient enhancement and the downward vertical velocity.

A second means by which GWs (either in addition to those discussed above or in isolation) could impact potential plasma instability seeding conditions is through vertical motions largely without accompanying enhanced electron density gradients. This occurs for GWs approaching a turning level, and it is especially likely for the large-amplitude and large vertical wavelength GWs at high intrinsic frequencies propagating westward in an eastward tidal shear (with $U_{\rm tide}$ increasing eastward with altitude). As a GW approaches a turning level, amplitude growth abates and $m$=>0, resulting in the GW motions becoming largely vertical in nature and causing only small electron density fluctuations, despite potentially large vertical displacements. We also know this must be an important process in the lower thermosphere, as it is exactly this mechanism that accounts for the continuous removal of the higher-frequency GWs at the smallest remaining horizontal wavelengths from the spectrum of westward-propagating GWs in an eastward shear or with decreasing N with altitude (FV08). Indeed, the vertical velocities that would arise in this scenario would likely by comparable to or may exceed those associated with the vertically-propagating GWs discussed above (as large as ∼20 to 50 ms$^{-1}$). Indeed, evidence for exactly this process can be seen in the analysis of PFISR data by Vadas and Nicolls (2008). This scenario is depicted in the lower panel of Fig. 6 and the possible plasma instability parameter impacts are estimated in the lower portion of Table 6. Such motions would also have westward phase velocities potentially close to the westward

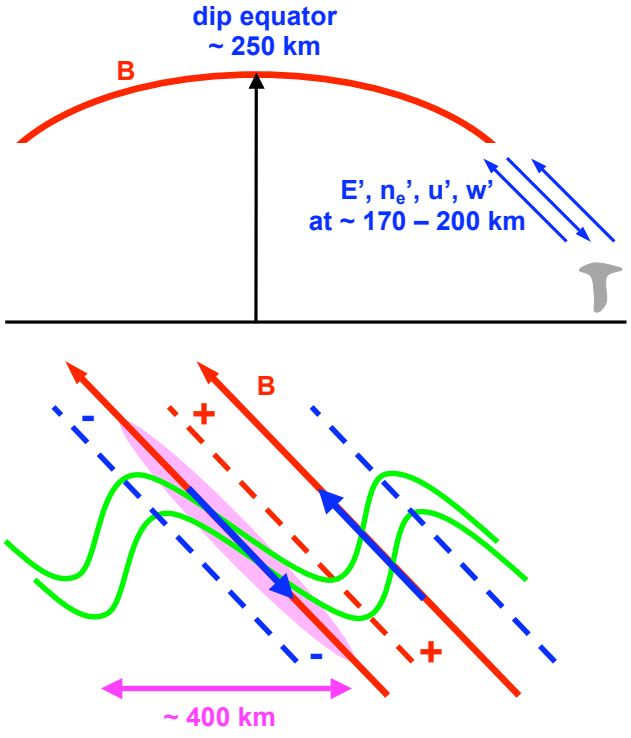


**Fig. 7.** Schematic cross section along the magnetic field showing GW velocity perturbations and phase orientation (top panel, blue arrows) arising from deep convection and aligned along the magnetic field. GW velocity, temperature (bottom panel; dashed lines, red positive, blue negative), and electron density per unit mass (green) and electron density gradient perturbations (pink positive) off the dip equator at altitudes providing an enhanced field line-integrated electron density gradient along the downward phase of the GW. Polarization electric fields will also arise, but may not contribute to plasma perturbations if they short out to lower altitudes.

plasma drifts. And if so, they would enable coherent vertical perturbations of much longer duration than suggested by the observed, or intrinsic, GW periods.

#### 3.2.4 Superposed GW and tidal structures off the dip equator

We assumed above that the largest and most likely GW contributions to plasma instability growth rates would include simultaneous negative vertical velocities, large eastward winds, and enhanced electron density gradients in the presence of eastward tidal winds at the bottomside F layer near the dip equator. These are expected to accompany primarily westward-propagating GWs, as these most easily attain high altitudes in the presence of eastward tidal winds. There are other ways for GWs to influence plasma instability growth rates, however, if their effects can be communicated up the field lines from locations at lower altitudes off the dip equator with sufficient field line-integrated magnitudes.

Assuming that 1) plasma perturbations at the bottomside F layer and below are driven by local neutral and plasma dynamics and 2) plasma instabilities are sensitive to field-line-integrated contributions, we may expect that neutral dynamics can make distinct (and simultaneous) contributions to plasma instability growth rates at different locations and altitudes. The primary means by which GW activity off the dip equator at somewhat lower altitudes could contribute to modulation of plasma instability growth rates would be through enhanced field line-integrated electron density gradients or wind-driven polarization electric fields. These could occur in several ways, as GW propagation against weaker tidal winds is not as important at lower altitudes (see Fig. 5), thus allowing GWs propagating in various directions to contribute. The same arguments also apply for GWs reaching the bottomside F layer, but having propagation along, rather than normal to, the magnetic field nearer to the dip equator. We note, however, that Prakash and Pandey (1985) and Kelley (1989) also recognized the potential for strong dependence on GW propagation directions, with perturbations along field lines causing electric fields that short out to lower altitudes.

From Tables 1, 4, and 5 we see that a GW having a horizontal wind perturbation of $u_h' \sim 1\,\mathrm{ms}^{-1}$ at $\sim 80\,\mathrm{km}$ can achieve horizontal wind and plasma density gradient perturbations of $u_h' \sim 50\,\mathrm{ms}^{-1}$ and $(H_e/\rho_e)\partial\rho_e'/\partial z \sim 100\%$, respectively, at $\sim 200\,\mathrm{km}$ under mean solar conditions for a range of propagation conditions. This also implies that the range of GW intrinsic frequencies that may contribute is also more extended, and in particular, that lower-frequency GWs can play potentially larger roles than at higher altitudes. To have the greatest field-line-integrated effect, a GW at lower altitude would need to have its phase structure aligned along the slanted magnetic field for some significant distance (Fig. 7, top). This would occur for a GW propagating upward towards the dip equator, and a GW frequency of $\omega \sim N/10$ to $N/5$ would readily allow a conducive phase structure to coincide with a field line for several 100s of km, given typical GW scales. In this case, the GW would contribute potentially large field-line-integrated enhancements of the electron density gradient where GW velocities are downward and poleward (Fig. 7, bottom, pink region where the blue arrow is downward).

## 4 Summary and conclusions

We have employed SpreadFEx measurements and associated modeling to estimate GW and tidal perturbations at the bottomside F layer that appear to have a potential to impact plasma instability processes and the seeding of plasma bubbles extending to higher altitudes. GW spatial and temporal scales and perturbation amplitudes were inferred from neutral and electron density measurements in the lower atmosphere and ionosphere, respectively. The spatial and temporal scales were confirmed to be those expected at TI altitudes

by viscous ray tracing. Ray tracing also demonstrated the effects of GW refraction by thermospheric winds and amplitude growth due to decreasing densities, including the survival to high altitudes of only those GWs propagating westward against the eastward tidal winds at times of plasma bubble seeding and the attainment of potentially large amplitudes at higher altitudes. Continued refraction of the highest-frequency westward-propagating GWs in an eastward tidal wind shear at the bottomside F layer also has a potential to allow large vertical motions accompanying GWs approaching a turning level having additional influences on plasma instabilities at the bottomside F layer.

Tidal horizontal motions were estimated to be ∼50 to 100 $ms^{-1}$ at the bottomside F-layer, with fractional neutral and electron densities of ∼2 to 10% and ∼5 to 20%, respectively, and fractional electron density gradients that are comparable. GWs were estimated to achieve horizontal and vertical perturbation velocities of ∼50 to 100 $ms^{-1}$ and ∼30 to 50 $ms^{-1}$ or more, respectively, with fractional neutral and electron densities of ∼5 to 10% and ∼20 to 40%, respectively, and fractional electron density gradients of ∼40% or larger. Thus, tidal and GW perturbations at the bottomside F layer appear to achieve sufficient magnitudes and apparent phase structures to substantially enhance plasma instability growth rates and contribute to plasma bubble seeding. Our most important finding, however, is that superposed GW and tidal structures appear to have the potential to simultaneously enhance all of the terms that contribute to plasma instability growth rates in a common volume. This results from the different contributions by tides, and GWs of varying intrinsic frequencies, to the various relevant fields. Whereas tidal winds dominate the horizontal motion field, only GWs contribute significantly to neutral vertical motions. Tides and GWs also contribute very differentially to perturbation electron density gradients because of their different vertical wavelengths and time scales. This allows for superpositions of tidal and GW fields that have regions in which eastward and downward winds and vertical electron density gradients are correlated and simultaneously enhanced. GWs may also easily enhance field-line-integrated electron density gradients or polarization electric fields through phase alignment along the magnetic field at lower altitudes off the dip equator. There may be adverse effects of such alignments, however, such as the shorting of electric fields at lower altitudes. The implications of these GW and tidal perturbations and their correlations for plasma instability growth rates are examined analytically and numerically by Abdu et al. (2008) and Kherani et al. (2008).

*Acknowledgements.* The SpreadFEx field program and data analysis were supported by NASA under contracts NNH04CC67C, NNH07CC81C, and NAS5-02036. Related modeling and theoretical activities were supported by NSF grants ATM-0314060, ATM-0436703, and ATM-0537311 and AFOSR contract FA9550-06-C-0129. Some of the authors also had partial support from Conselho Nacional de Desenvolvimento Cientifico e Tecnologico CNPq (Abdu, Sobral, de Paula, I. Batista, Takahashi, and Gobbi). We also thank Dave Hysell for valuable discussions and two anonymous reviewers for very useful comments that improved our paper.

Topical Editor U.-P. Hoppe thanks two anonymous referee for their help in evaluating this paper.

## References

Abdu, M. A., Kherani, E. A., Batista, I. S., de Paula, E. R., and Fritts, D. C.: An evaluation of the ESF/bubble irregularity growth conditions under gravity wavbe influences based on observational data from the SpreadFEx campaign, SpreadFEx special issue, Ann. Geophys., in review, 2008.

Beer, T.: Spatial resonance in the ionosphere, Planet. Space Sci., 21, 297–307, 1973.

Comberiate, J. M., Kamalabadi, F., and Paxton, L. J.: A tomographic model for ionospheric imaging with the Global Ultraviolet Imager, Radio Sci., 42, RS2011, doi:10.1029/2005RS003348, 2007.

Earle, G. D., Musumba, A. M., and Vadas, S. L.: Satellite-based measurements of gravity wave-induced midlatitude plasma density perturbations, J. Geophys. Res., 113, A03303, doi:10.1029/2007JA012766, 2008.

Fejer, B. G.: Natural ionospheric plasma waves, in: Modern Ionospheric Science, edited by: Kohl, H., Rüster, R., and Schlegel, K., pp. 217–273, Max-Planck Institut für Aeronomie, Lindau, Germany, 1996.

Fritts, D. C. and Vadas, S. L.: Gravity wave penetration into the thermosphere: Sensitivity to solar cycle variations and mean winds, Ann. Geophys., in review, 2008.

Fritts, D. C., Abdu, M. A., Batista, B. R., Batista, I. S., Batista, P. P., Buriti, R., Clemesha, B. R., Comberiate, J., Dautermann, T., de Paula, E., Fechine, B. J., Fejer, B., Gobbi, D., Haase, J., Kamalabadi, F., Laughman, B., Lima, P. P., Liu, H.-L., Medeiros, A., Pautet, D., São Sabbas, F., Sobral, J. H. A., Stamus, P., Takahashi, H., Taylor, M. J., Vadas, S. L., and Wrasse, C.: Overview and Summary of the Spread F Experiment (SpreadFEx), Ann. Geophys., in review, 2008a.

Fritts, D. C., Abdu, M. A., Batista, B. R., Batista, I. S., Batista, P. P., Buriti, R., Clemesha, B. R., Comberiate, J., Dautermann, T., de Paula, E., Fechine, B. J., Fejer, B., Gobbi, D., Haase, J., Kamalabadi, F., Laughman, B., Lima, P. P., Liu, H.-L., Medeiros, A., Paute, D., São Sabbas, F., Sobral, J. H. A., Stamus, P., Takahashi, H., Taylor, M. J., Vadas, S. L., and Wrasse, C.: The Spread F Experiment (SpreadFEx): Program overview and first results, Earth Planets Space, in press, 2008b.

Fritts, D. C. and Alexander, M. J.: Gravity dynamics and effects in the middle atmosphere, Rev. Geophys., 41, 8755–1209, doi:10.1029/2001RG000106, 2003.

Haase, J., Dautermann, T., Taylor, M., Chapagain, N., Calais, E., and Pautet, D.: Propagation of plasma observed in Brazil from GPS and airglow data, Ann. Geophys., in review, 2008.

Hysell, D. L., Kelley, M. C., Swartz, W. E., and Woodman, R. F.: Seeding and layering of equatorial spread F by gravity waves, J. Geophys. Res., 95, 17 253–17 260, 1990.

Hysell, D. L. and Kudeki, E.: Collisional shear instability in the equatorial F region ionosphere, J. Geophys. Res., 109, A11301, doi:10.1029/2004JA010636, 2004.

Kamalabadi, F., Karl, W. C., Semeter, J. L., Cotton, D. M., Cook, T. A., and Chakrabarti, S.: A statistical framework for space-based EUV ionospheric tomography, Radio Sci., 34(2), 437–447, 1999.

Kamalabadi, F., Bust, G., Dymond, K., Gonzalez, S., Bernhardt, P., Chakrabarti, S., Cotton, D., Stephan, A., McCoy, R., Budzien, S., and Thonnard, S.: Tomographic studies of aeronomic phenomena using radio and UV techniques, J. Atmos. Solar-Terres. Phys., 64(12), 1573–1580, 2002.

Kamalabadi, F., Comberiate, J., and Taylor, M.: Electron densities in the lower thermosphere from GUVI 1356 tomographic inversions in support of SpreadFEx, Ann. Geophys., in review, 2008.

Kelley, M. C.: The Earth's Ionosphere, Academic Press, San Diego, 487 pp, 1989.

Kelley, M. C., Larsen, M. F., Lahoz, C., and McClure, J. P.: Gravity wave initiation of equatorial spread F – A case study, J. Geophys. Res., 86, 9087–9100, 1981.

Kherani, A., Abdu, M., Paula, E., et al.: 3-D simulations of plasma instabilities employing SpreadFEx estimates of gravity wave parameters for seeding conditions, Ann. Geophys., in review, 2008.

Klostermeyer, J.: Nonlinear investigation of the spatial resonance effect in the nighttime equatorial F region, J. Geophys. Res., 83, 3753–3760, 1978.

Kudeki, E., Akgiray, A., Milla, M., Chau, J. L., and Hysell, D. L.: Equatorial spread-F initiation: post-sunset vortex, thermospheric winds, gravity waves, J. Atmos. Solar-Terr. Phys., 69, 2416–2427, 2007.

McClure, J. P., Singh, S., Bamgboye, D. K., Johnson, F. S., and Kil, H.: Occurrence of equatorial F region irregularities: Evidence for tropospheric seeding, J. Geophys. Res., 103, 29 119–29 135, 1998.

Meriwether, J., Faivre, M., Fesen, C., Sherwood, P., and Veliz, O.: New results on equatorial thermospheric winds and the midnight temperature maximum, Ann. Geophys., 26, 447–466, 2008, http://www.ann-geophys.net/26/447/2008/.

Prakash, S. and Pandey, R.: Generation of electric field due to gravity wave winds and their transmission to other ionospheric regions, J. Atmos. Terr. Phys., 47, 363–374, 1985.

Rodrigues, F., Hysell, D. L., and de Paula, E. R.: Coherent radar backscatter imaging in Brazil: Large-scale waves in the bottomside F region at the onset of equatorial spead F, Ann. Geophys., to be submitted, 2008.

São Sabbas, F., Rampinelli, V. T., Santiago, J., Stamus, P., Vadas, S., Taylor, M. J., Neto, G. D., Pinto, O., and Fritts, D.: Characteristics of sprite and possible gravity wave convective sources present on satellite IR images for the SpreadFEx 2005 campaign, Ann. Geophys., in review, 2008.

Sekar, R. and Kelley, M. C.: On the combined effects of vertical shear and zonal electric field patterns on nonlinear equatorial spread F evolution, J. Geophys. Res., 103, 20 735–20 747, 1998.

Swartz, W. E. and Woodman, R. F.: Same night observations of spread-F by the Jicamarca Radio Observatory in Peru and CUPRI in Alcantara, Brazil, Geophys. Res. Lett., 25, 17–20, 1998.

Takahashi, H., Taylor, M. J., Pautet, P.-D., Medeiros, A. F., Gobbi, D., Wrasse, C. M., Fechine, J., Abdu, M. A., Batista, I. S., Paula, E., Sobral, J. H. A., Arruda, D., Vadas, S., Sabbas, F. S., and Fritts, D.: Simultaneous observation of ionospheric plasma bubbles and mesospheric gravity waves during the SpreadFEx Campaign, Ann. Geophys., in review, 2008.

Taylor, M. J., Pautet, P. D., Medeiros, A. F., Buriti, R., Fechine, J., Fritts, D. C., Vadas, S., Takahashi, H., and Sao Sabbas, F.: Characteristics of mesospheric gravity waves near the magnetic equator, Brazil, during the SpreadFEx campaign, Ann. Geophys., in press, 2008.

Vadas, S. L.: Horizontal and vertical propagation, and dissipation of gravity waves in the thermosphere from lower atmospheric and thermospheric sources, J. Geophys. Res., 112, A06305, doi:10.1029/2006JA011845, 2007.

Vadas, S. L. and Fritts, D. C.: Thermospheric responses to gravity waves arising from mesoscale convective complexes, J. Atmos. Solar Terr. Phys., 66, 781–804, 2004.

Vadas, S. L. and Fritts, D. C.: Thermospheric responses to gravity waves: Influences of increasing viscosity and thermal diffusivity, J. Geophys. Res., 110, D15103, doi:10.1029/2004JD005574, 2005.

Vadas, S. L. and Fritts, D. C.: The influence of increasing temperature and solar variability on gravity wave structure and dissipation in the thermosphere, J. Geophys. Res., TIMED special issue, 111, A10812, doi:10.1029/2005JA011510, 2006.

Vadas, S. L. and Fritts, D. C.: Reconstruction of the gravity wave field excited by convective plumes via ray tracing in real space, Ann. Geophys., in review, 2008.

Vadas, S. L. and Nicolls, M. J.: Temporal evolution of neutral, thermospheric winds and plasma response using PFISR measurements of gravity waves, PFISR special issue, J. Atmos. Solar-Terr. Phys., in press, 2008.

Vadas, S. L., Fritts, D. C., Pautet, P.-D., Taylor, M. J., Liu, H.-L., Batista, P. P., Takahashi, H., Sao Sabbas, F., Stamus, P., Medeiros, A. F., Buriti, R., and Fechine, J.: Amplitudes, scales, and variability of gravity waves in the thermosphere from convective plumes over Brazil, Ann. Geophys., submitted, 2008a.

Vadas, S. L., Taylor, M. J., Pautet, P.-D., Stamus, P., Fritts, D. C., São Sabbas, F., and Rampinelli, V. T.: Convection: The likely source of the medium-scale gravity waves observed in the OH airglow layer near Brasilia, Brazil, Ann. Geophys., in review, 2008b.

Vargas, F., Gobbi, D., and Takahashi, T.: Gravity wave amplitudes and momentum fluxes inferred from OH airglow intensities and meteor radar winds during SpreadFEx, Ann. Geophys., in review, 2008.

Whitehead, J. D.: Ionization disturbances caused by gravity waves in the presences of an electrostatic field and background wind, J. Geophys. Res., 76, 238–241, 1971.

Wrasse, C. M., Takahashi, H., Fechine, J., Medeiros, A. F., and Bageston, J. V.: Ray tracing of GWs observed in OH airglow during SpreadFEx, Ann. Geophys., in review, 2008.